Crystal structure and phase transitions of layered perovskite-like $CsScF_4$ crystal

A.S. Krylov,[a] M.S. Molokeev,[a;b] S.V. Misyul,[c] S.N. Krylova,[a] A.S. Oreshonkov,[a;c] A.A. Ivanenko,[a] V.A. Zykova,[d] Yu.I. Ivanov,[a] A:A: Sukhovsky ,[a] V.N. Voronov,[a] I.N. Safonov,[c] and A.N. Vtyurin[a;c]

This work is devoted to the complex research of temperature phase transitions in $CsScF_4$ crystal. Crystal structure was solved and refined at different temperatures by Rietveld method. Structural phase transitions were investigated by spectroscopic methods some of them for the first time: Brillouin spectroscopy, Raman spectroscopy, IR absorption spectroscopy and NMR. The symme-try analysis of the center Brillouin zone of all phases is presented. The vibrational spectra of the crystal in three phases have been calculated. The structural phase transitions mechanism was determined. The transitions at T_1 = 475 K and T_2 = 317.5 K are of displacement type. The Raman soft modes have been associated with rotations of ScF_6 octahedral group.

1 Introduction

The crystals whose high symmetry phase belongs to the space group D^1_{4h} P4=mmm have been under intensive scrutiny in re-cent few years. Among them, the layered perovskite-like com-pounds with a $TlAlF_4$-type structure are remarkable for retaining the infinite chains of vortex-sharing octahedra as an essential fea-ture of the perovskite structure. Several compounds of the series exhibit phase transitions (PT) to a superconductive state, for ex-ample, Tl – Ca– Ba– Cu – O compounds containing constituents with a high-temperature superconductive phase. [1,2]

ABX_4 crystals with a $TlAlF_4$-type structure are known to have compounds where A position is taken by zigzag polyethylenedi-ammonium ions $[NH_3(CH_2)_nNH_3]^+$ essentially increasing the dis-tances between the layers of connected octahedral groups BX_6. [3] The structure of such compounds was studied [3] for chlorides with B = Mn, Cd, Cu and n = 2 5. Many of the mentioned com-pounds have sequences of phase transitions. (see [1,4–6]). Earlier phase transitions in crystals of $MAlF_4$ family (M = Tl, K, Rb, NH_4) were studied by various techniques (Brillouin and ultrasonic, [7,8] Raman [9,10], Raman under high hydrostatic pressure, [11,12] neu-tron scattering, [13] group theory, [14] Monte Carlo simulation [15]). Sc-containing layered perovskites have not been widely studied. In-deed, some of Sc layered perovskites have interesting physical properties such as surprisingly large negative thermal expansion coefficients which exist over a wide range of temperatures. [16–18]

Symmetry and crystallographic analyses of phase transition se-quences in layered $TlAlF_4$-type crystals were better described in [5] where it was pointed out that such structures realize mostly rotary distortions or pivot-type distortions caused by rotation of octahe-dral groups BX_6. The order parameters (OP) corresponding to librational vibrations of the octahedra are transformed according irreducible representation (IR) of M (k18) and X (k150) bound-ary points of Brillouin zone of D^1_{4h} P4=mmm group (denotations according to ref. [19,20]) Distortions associated with condensation of librational modes of M and X points are denoted in [5] as dis-tortions of f and y types. Irreducible representations and order parameters inducing symmetry changes are commonly referred to as critical or primary.

However, in some cases distortion of the initial phase structure cannot be described by the critical order parameters only. In dis-torted (disymmetric) phase, shifts or ordering of atoms should be consistent with the symmetry of this phase and determined by

[a] *L.V. Kirensky Institute of Physics SB RAS, 660036, Krasnoyarsk, Russia E-mail: shusy@iph.krasn.ru*
[b] *Department of Physics, Far Eastern State Transport University, 680021, Khabarovsk, Russia*
[c] *Institute Engineer Physics and Radioelectronics, Siberian Federal University, 660041, Krasnoyarsk, Russia*
[d] *Institute of Automation and Electrometry SB RAS, 630090, Novosibirsk, Russia*

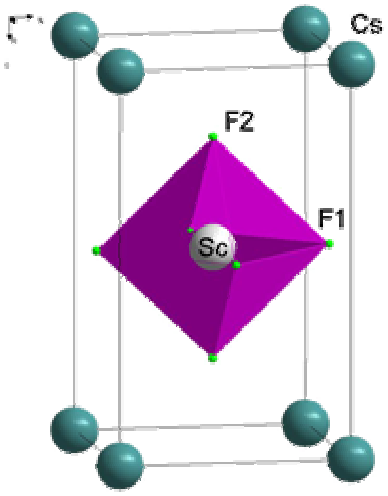

Fig. 1 Crystal structure of $CsScF_4$ at P4=mmm phase.

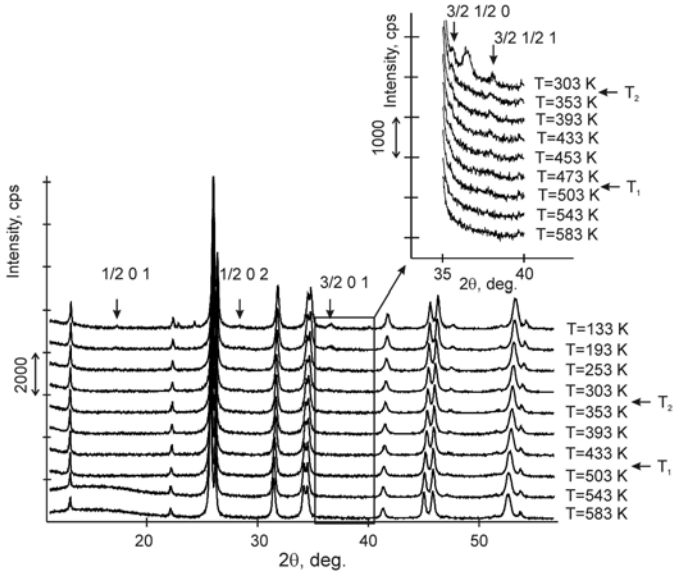

Fig. 2 X-ray diffraction patterns in 2q region 11-56 of $CsScF_4$ from 133 to 583 K. At T_2=317.5 K several superstructure reflections corresponding X-point of Brillouin zone occur. Inset: Superstructure reflections corresponding to M-point of the Brillouin zone emerge with cooling. Indices of all superstructure peaks were calculated using cell parameters of parent phase and therefore they are rational numbers.

non-critical (secondary) order parameters and irreducible representations. The entire totality of order parameters – critical and noncritical – occurring during phase transition forms complete order parameter condensate. [21] Group theory analysis [5] of com-plete order parameter condensate in crystals with P4/mmm par-ent phase showed that critical distortions of f and y types could be accompanied by noncritical distortions of octahedral groups and noncritical shifts of atoms located between the layers of oc-tahedral groups. Such shifts and distortions are of a secondary nature and could be rather small in the proximity of the phase transition points.

The phase transition sequence in a $CsScF_4$ crystal was stud-ied by optical, calorimetric, X-ray and Raman scattering meth-ods. [6,22] It was found [6] to undergo two phase transitions under decreasing temperature; the respective temperatures and basic thermodynamic characteristics are given in Table 1. The experimental data [6,22] gave grounds to make the following conclusions:

1) both phase transitions in $CsScF_4$ are of a displacement type,

2) the phase transition from G_0 to G_1 is of the first order and from G_1 to G_2 is of the second order, 3) distortions are of the form $(00Y_z)$ at phase transition G_0 ! G_1 , at phase transition G_1 ! G_2 - $(F_1F_2Y_z)$.

However, these conclusions about the form of distortions at the phase transitions was based on indirect data. Besides, conspicuous is the temperature dependence of superstructure reflections occurring in the monoclinic phase which could not be explained by the rotations of octahedral groups only. [6]

To answer the arising questions, experimental Raman scattering, nuclear magnetic resonance and X-ray diffraction studies of $CsScF_4$ crystal have been carried out over a broad temperature range including phase transition temperatures. To interpret the results of the studies, the phase transition sequence was described within thermodynamical approach..

2 Experimental

A clear and transparent $CsScF_4$ crystal was grown by Bridgman method in a platinum ampoule. The crystal grown had an ideal basal plane $(001)_0$.

At room temperature, $CsScF_4$ single crystals have multiple twins, therefore the powder X-ray diffraction (XRD) was studied with a Bruker D8 ADVANCE Bragg-Brentano diffractometer using Cu-Ka radiation. The beam was controlled by a 0.6 mm fixed di-vergence slit, 6mm receiving VANTEC slit and Soller slits. Low-and high-temperature measurements were taken with an Anton Paar TTK450 attachment.

The variable counting time (VCT) and step size (VSS) schemes were used to collect the diffraction data. The total experimental time was 5 hours. There were 10 such experiments performed at different temperatures from 133 to 583 K were measured (Fig. 2).

An X-ray analysis of the $CsScF_4$ structure at room temperature showed that the crystals grown were free from any impurities. The main structural reflections were found to coincide with the orthorhombic symmetry suggested in [5,34].

Raman spectra in the backscattering geometry were recorded in

a subtractive dispersion mode with a Horiba Jobin Yvon T64000 triple spectrometer equipped with a liquid nitrogen cooled charge coupled device detection system. Specrta-Physics Stabilite Ar^+ ion laser 2017 with l = 514.5 nm and power 5 mW on the sample was used as an excitation light source.

Temperature measurements were carried out with closed cycle ARS CS204-X1.SS helium cryostat in the temperature range 10 – 295 K. The temperature was monitored by LakeShore DT-6SD1.4L silicon diode. During experiments the cryostat was evacuated to 10^{-6} mbar. To investigate the low-wavenumber spectra, measure-ments down to 6 cm^{-1} were performed in a subtractive disper-sion mode. Deformation of the low-wavenumber spectral edge by the optical slit, which sometimes smears the true features of low-wavenumber spectra, was carefully eliminated by rigorous optical alignmeat. The CCD pixel coverage in additive dispersion mode was as fine as 0.3 cm^{-1} but it was limited by the spectrometer spectral resolution of 1.8 cm^{-1}.

The temperature experiments were carried out in a dynamic mode varying the sample temperature at the rate 0.5 K/min. The uncertainty of the measured temperature for a given rate can be estimated as the difference between the adjacent measurements and it was 0.12 K in one spectrum measurement. The overall time for a single spectrum accumulation was within 30 s. The spectra were acquired with a temperature step 0.25 K. This mea-surement protocol was the same as described in ref.[27,28]

The high temperature (above 320K) and polarized Raman ex-periments were carried out using a laser beam focused on the sample by an 50x Olympus LMPlanFI objective lens with a numer-ical aperture (NA) of 0.5. The power of the incident laser light was 5 mW on the sample. The scattered light was collected by the same objective lens in a backscattering geometry and analyzed us-ing a polarizer and l -plate. The temperature of the samples was controlled by a Linkam THMS600 microstat with the stability of < 0.2 K.

Infrared spectra were obtained in the temperature range from 15 to 300 K using vacuum Vertex 80 spectrometer. The 3 3 mm and 50 mm thick crystal plate and was used as a sample.

NMR studies of $CsScF_4$ crystals were carried out on all magnetic nuclei in the crystal. NMR spectra of ^{19}F, ^{45}Sc and ^{133}Cs nuclei were recorded with an AVANCE 300 pulse NMR spectrometer by Fourier spectroscopy (Larmor frequencies for ^{19}F nuclei – 282.4 MHz, for ^{45}Sc nuclei – 72.9 MHz, and for ^{133}Cs nuclei – 39.4 MHz, 90 pulse time was 2.9 ms for fluorine and about 1 ms for scandium and cesium)

The Brillouin scattering spectra were measured in back scatter-ing with 3+3 pass Sandercock tandem Fabry-Perot interferome-ters.[29] The distance between the interferometer mirrors was 5 mm corresponding to the free dispersion range 30 GHz. The radiation source was a solid state 200 mW, 532 nm laser. The reference beam was isolated after reflection of the primary laser radiation from a thin glass plane and was used to adjust the spec-trometer and stabilize its operation during measurements. After passing the glass plane the characteristic laser radiation was di-rected by a prism (PR) (2 mm) onto the sample under study. An achromatic lens (L_1) with the focal length 150 mm both focused the radiation onto the sample and collected the scattered signal. The scattered radiation was focused on the input diaphragm of the spectrometer by a lens (L_2) with the focal length 400 mm. The size of the input and output diaphragms was 450 and 700 mm, respectively. The periscope mirrors M_1 and M_2 were used for vertical and horizontal adjustment to put the scattered radiation into the spectrometer.

3 Determination of crystal structures

Earlier[5] it was supposed that the crystal has phase transitions sequence $P4=mmm \xrightarrow{M3+(h)} P4=mbm \xrightarrow{M3+(h)\ X3+(x_1;x_2)} Pmmn$. We believe that these designations of irreducible representations (ir-rep) are incorrect. Really, M3 + (k18t3) and X3 + (k15t3) irreps lead to distortion of the ScF_6 octahedron (Fig. 3). The analy-sis shows that only M2 + (k18t5) and X2 (k15t8) lead to rota-tion of the ScF_6 octahedron (Fig. 3), so M2+ and X2 should be critical irreps instead. In addition, such a sequence of ir-reps agrees with the sequence of space groups $P4=mmm \xrightarrow{M2+(h)} P4=mbm \xrightarrow{M2+(h)\ X2\ (x_1;x_2)} Pmmn$[5] found earlier.

Comparison of powder diffraction data shows the structure to have changed at 460-475 K where superstructure peaks emerge corresponding to the M-point of Brillouin zone (Fig. 2) and at T_2=317.5 K where several superstructure peaks of the X-point of Brillouin zone emerge. This confirms that the phase transition at T_1=475 K is associated with the appearance of order parameter (OP) of the M irreducible representation and the next phase tran-sition at T_2=317.5 K is associated with OP of the X irreducible representation. As ScF_6 can be rotated by M2+ and X2 only, it was decided to refine the crystal structure considering M2+ and X2 as critical irreducible representations.

The crystal structure of the low temperature phases was solved by a distortion-mode refinement of the X-ray data using TOPAS 4.2 program, with the file generated by ISODISPLACE.[30,31] Space groups P4=mbm and Pmmn were used. There are two OPs asso-ciated with all displacements of atoms: GM1 + (a); M2 + (h) for the P4=mbm phase and nine OPs: GM1 + (a), M1 + (b), M2 + (h), six OPs X2 (x_1; x_2) for the Pmmn phase. M2+ acts on 2e sites occupied by F and leading to rotation of the ScF_6, X2 acts on F sites and Cs sites. M1+ leads to distortion of the ScF_6 octahedron. All the respective amplitudes were used to find a model structure by the simulated anneal method. The refinement yielded satis-factory final R-factors (Table 3), interatomic distances as well as thermal parameters. Rietveld difference plot of $CsScF_4$ at 303 K is shown in Fig. 4. All other results within the range 133–583 K are

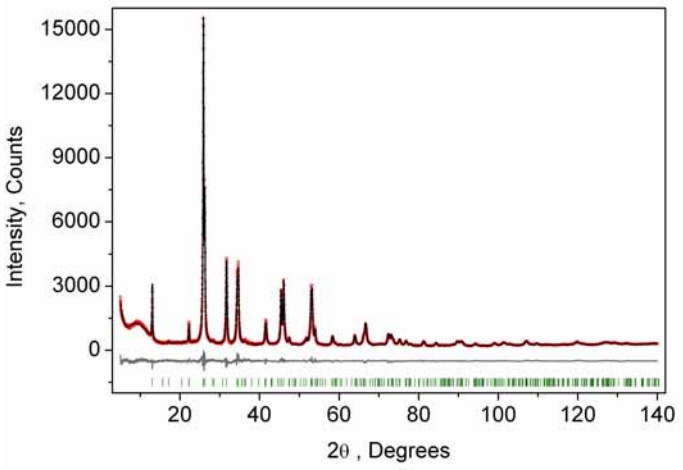

Fig. 4 Rietveld difference plot of $CsScF_4$ at 303 K (Pmmn phase). Other plot presented at ESI

given in ESI. The thermal parameter of Cs ion was refined in an anisotropic model. The atomic coordinates and isotropic thermal parameters can be found in Table 4 and the main bond lengths in Table 2. One can see that the thermal parameters rise evenly upon heating. This is indicative of the absence of any order-disorder process at phase transitions and proves the suggestion [5] that the mechanisms of phase transitions have a displacive distortion na-ture. The difference between the lengths of Sc-F bonds is small (maximum 0.115) and the F–Sc–F angles in the octahedron range within 87 93 . So the ScF_6 octahedron does not undergo strong distortions at phase transitions. This agrees with the earlier con-clusions [5,22,32–34].

Complete mode details of distorted structures show the follow-ing temperature dependences of displacive mode amplitudes (Fig. 5). It is obvious that OP (h) of M2+ irrep is critical as it has maximal values. It emerges jump wise at T_1 = 475 K which ac-counts for a first order transition, and increases upon further cool-ing. New critical OPs (h_1; x_2) appear at T_2=317.5 K and increase rapidly upon cooling. GM1 + (a) and M1 + (b) are noncritical.

The primitive cell volume is doubled at the first phase transi-tion $P4/mmm \xrightarrow{M3+(h)} P4/mbm$ (Fig. 6). The cell parameters are transformed: $a_1 = a_0 + b_0$; $b_1 = b_0\ a_0$; $c_1 = c_0$ (a_1; b_1; c_1 – are the basis vectors of the distorted P4/mbm phase, a_0; b_0; c_0 – ba-sis vectors of the parent P4/mmm phase), the origin shift is (1/2, 1/2, 0). The ScF_6 octahedrons with a common node are rotated on f h in opposite directions. There are no other rotations or heavy atom displacement.

At the second phase transition $P4/mbm \xrightarrow{M2+(h)\ X2\ (x_1;x_2)} Pmmn$ the primitive cell volume increases 4 times. Position 1a oc-cupied by Cs is split into two: Cs1 and Cs2. The cell parameters are transformed as follows: $a_2 = 2a_0$; $b_2 = 2b_0$; $c_2 = c_0$ (a_2; b_2; c_2

Fig. 3 Group-subgroup graph with possible distortion of ScF_6 octahedron. Phase transitions allowing rotation of ScF_6 octahedron are showed by bold line.

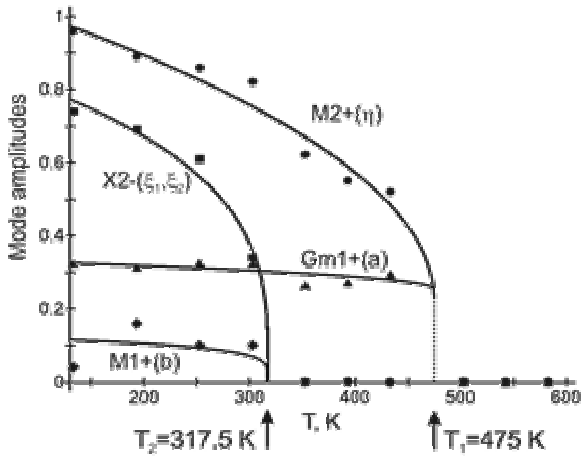

Fig. 5 Displacive mode amplitudes.

are the basis vectors of the distorted Pmmn phase, a_0; b_0; c_0 – basis vectors of parent P4=mmm phase). The rotation on f h goes on, and two new rotations are appear: around axis on angle a b

1 1 2 2

OPs (x_1; x_2) make the Cs1 and Cs2 atoms move along the c axis. A detailed analysis of the OP and irreps in the program ISOTROPY [30] shows that M2 + (h) and X2 (x_1; x_2) induce the phase transition that could be second order phase transition. In fact, the phase transition at T_1=475 K is of a first order type and at T_2=317.5 K, it is of a second order type. [5,22,32–34]

4 Vibrational spectroscopy

4.1 The selection rules

To describe the results of the Raman and infrared experiments, we performed a symmetry analysis of the vibrational modes in all phases. The selection rules, classification of modes, Wyckoff posi-tions, irreducible representations and Raman tensor for all three phases are represented in Table 5. The fractional atomic coordi-nates are taken from Table 4. The Raman mode representation for the tetragonal phase P4=mmm and the temperature above 475 K at Brillouin zone center is:

$$G_{Raman} = A_{1g} + E_g \quad (1)$$

The infrared mode representation is:

$$G_{IR} = 3A_{2u} + 4E_u \quad (2)$$

It is reasonable to expect two modes in the Raman spectra and seven active modes in the infrared spectra, and acoustic modes. The Raman mode representation for the tetragonal phase P4=mbm with at the temperature above 317.5 K and below 475 K at the

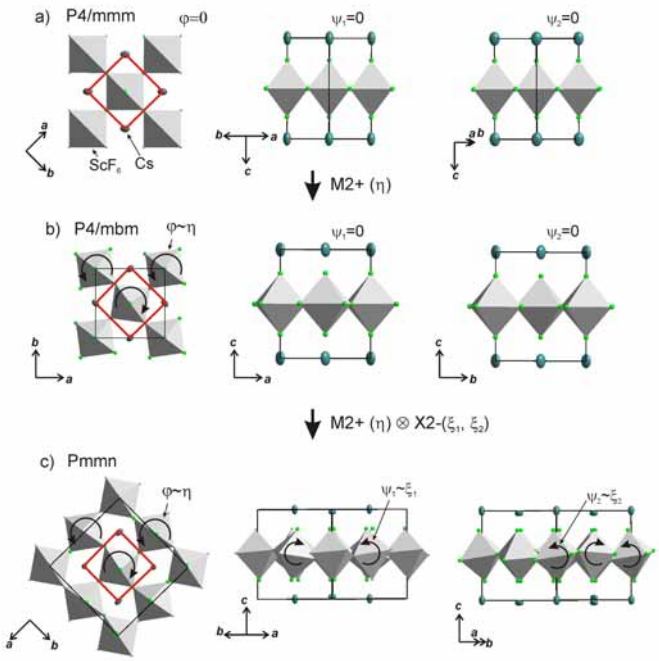

Fig. 6 Different projection of crystal structure: (a) tetragonal P4=mmm parent phase, ScF_6 doesn't rotate; (b) tetragonal P4=mbm distorted phase, ScF_6 rotates on f around c-axis; (c) orthorhombic Pmmn distorted phase, ScF_6 rotates on f around c-axis and rotates on y_1; y_2 around a + b axis and a b axis respectively.

Brillouin zone center is:

$$G_{Raman} = 2A_{1g} + B_{1g} + B_{2g} + 3E_g \quad (3)$$

The infrared mode representation is:

$$G_{IR} = 3A_{2u} + 7E_u$$

It is reasonable to expect 7 modes in the Raman spectra and 10 active modes in the infrared spectra, and acoustic modes. The Raman mode representation for the orthorhombic phase Pmmn and the temperature below 317.5 K at Brillouin zone center:

$$G_{Raman} = 9Ag + 5B_{1g} + 8B_{2g} + 8B_{3g} \quad (5)$$

the infrared mode representation is:

$$G_{IR} = 11B_{1u} + 10B_{2u} + 10B_{3u}$$

It is reasonable to expect 30 modes in the Raman spectra and 31 active modes in the infrared spectra, and 3 acoustic modes.

4.2 Raman and IR

To analyze the low wavenumber Raman spectra quantitatively, we performed a spectral analysis with a combination of conventional damped harmonic oscillator functions:[35,36]

$$I(w) = F(w; T) \sum_i \frac{2A_i w_{0i}^2 g_i w}{(w_{0i}^2 - w^2)^2 + 4g_i^2 w^2} \quad (6)$$

where w_0 is the current wavenumber, A, w and G denote the intensity, harmonic wavenumber of the band centre and full width at half maximum, respectively, of the corresponding excitation indicated by the subscript. The temperature factor F(w; T) is calculated by

$$F(w; T) = \begin{cases} n(w) + 1 & \text{Stokes} \\ n(w) & \text{Anti-Stokes} \end{cases} \quad (8)$$

$$n(w) = \frac{1}{\exp\left(\frac{\hbar w}{k_B T}\right) - 1} \quad (9)$$

where $\hbar$, k_B and c in (9) are denote the reduced Planck constant, and the Boltzmann constant, speed of light respectively. The present Raman setup can see only the Stokes component.

sult a part of vibrations from M point become Raman-active. We observe seven vibrations: 32 cm^{-1} (E_g), 107 cm^{-1} (A_{1g}), 152 cm^{-1} (E_g), 188 cm^{-1} (B_{1g}), 233 cm^{-1} (E_g), 255 cm^{-1} (B_{2g}), 495 cm^{-1} (A_{1g}). These vibrations are not associated with vibrations of heavy ions, but for these vibrations of fluorine ions only (Table 5). The experimental Raman data, numerical simulation and normal vibrational modes representations for P4=mbm phase can be found in Table 9

An overview of the experimental spectra of all components of the Raman tensor in all phases is shown in Fig. 7. The temper-atures of the spectra in the picture were chosen rather far from the phase transition points. The spectra of the intermediate phase P4=mbm at 393 K are fairly good agreement with the ones previ-ously published.[32]

The condensation of soft modes after both phase transitions is a most significant observed result, which is presented in Fig. 8. Dependences wavenumber vs. temperaturesare shown in Fig.

9. The Raman spectra include several modes demonstrating soft mode behavior: one (E_g 33 cm^{-1} at 393 K) below the first phase transition at T_1 = 478 K and two (A_g 37 cm^{-1} and 56 cm^{-1} at 193 K) below the second phase transition at T_1 = 317.5 K. These data are in a good agreement with the conclusion based on the XRD experiments. The results of empirical vibrational spectra simulation show that these soft modes correspond to rotations of the ScF_6 octahedral group (see Table 10).

Transformation of the IR spectra with temperature below 700 cm^{-1} is shown in Figure 10. Table 6 compares the experimental and calculated data for crystal in the Pmmn phase.

4.3 Vibrational spectra simulation

The lattice dynamics of $CsScF_4$ in all phases was simulated in terms of Born-Karman model using LADY software[37,38]. Within this model, only pair-wise interactions and bond-stretching force constants are considered. A simplified version of the Born-Karman model implies that the bond-stretching force constants A depend on R only (R is the bond length), and the A(R) dependences are the same for all atom pairs:

$$A = l e^{\left(\frac{R_{ij}}{r}\right)}; \quad (10)$$

where l and r are the parameters describing interaction of selected pairs. To find the parameters of the model a special

The high symmetry phase studied earlier by Raman spectra[32] exhibits two vibrations in spectrum: at 495 cm^{-1} (A_{1g}) and 152 cm^{-1} (E_g) just as was predicted by the selection rules (Table 5). The experimental Raman data, numerical simulation and normal vibrational modes representations for the P4=mmm phase are given in Table 8. These vibrations are the vibrations of axial fluorine atoms. After the first phase transition vibrations emerge mostly because of restructuring of the Brillouin zone; as a re-

optimization software was written and tested for several compounds.[39–45] The initial values of the parameters were set within the ranges typical for perovskite-like fluorides. The lattice stability conditions were taken into account. The final model parameters were obtained by minimization of residual values of the simulated and experimental Raman wavenumbers by Fletcher-Reeves method. In the case of optimization pending due to incompatibility of the model parameters, the initial parameters of the model

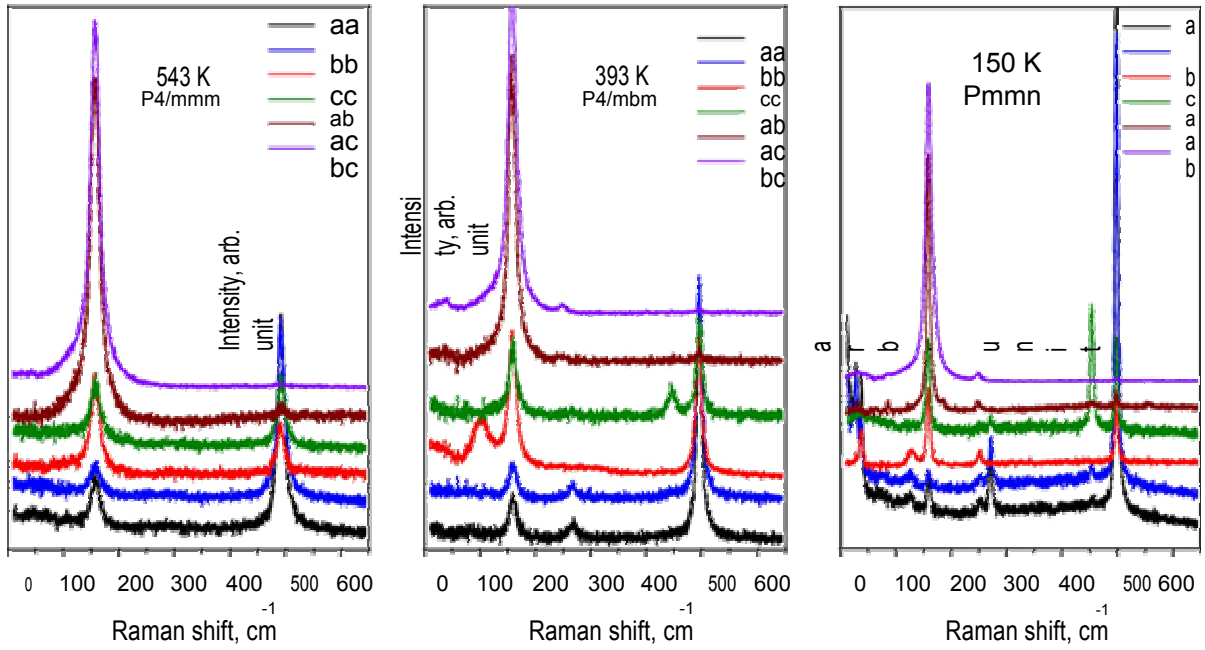

Fig. 7 Polarized Raman spectra a – P4=mmm, b – P4=mbm, c – Pmmn.

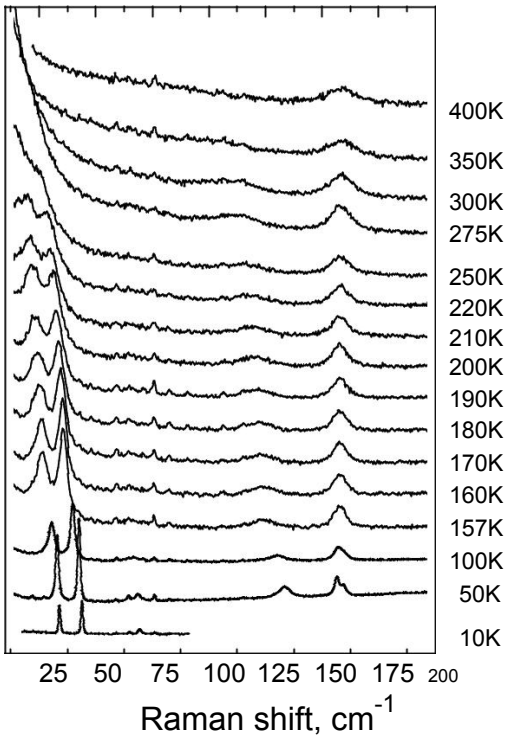

Fig. 8 Temperature evolution of Raman spectra of $CsScF_4$. Arrow indicate the soft modes

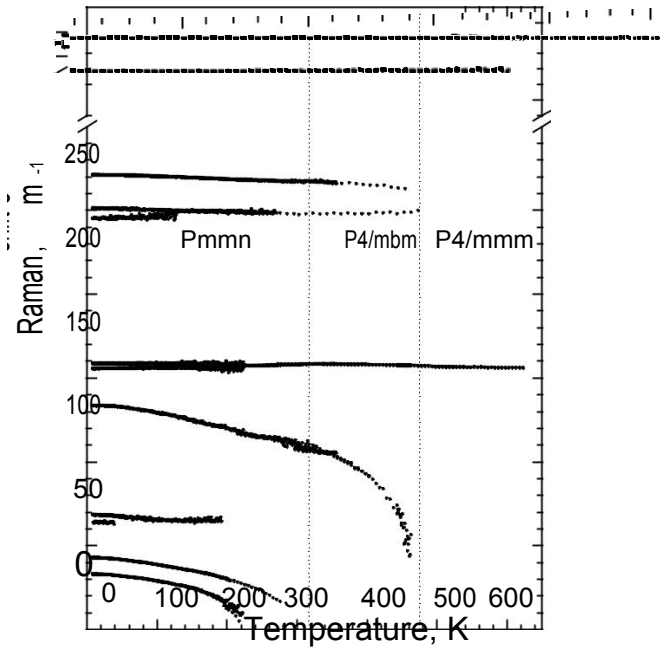

Fig. 9 Temperature dependence of the most intensive Raman lines

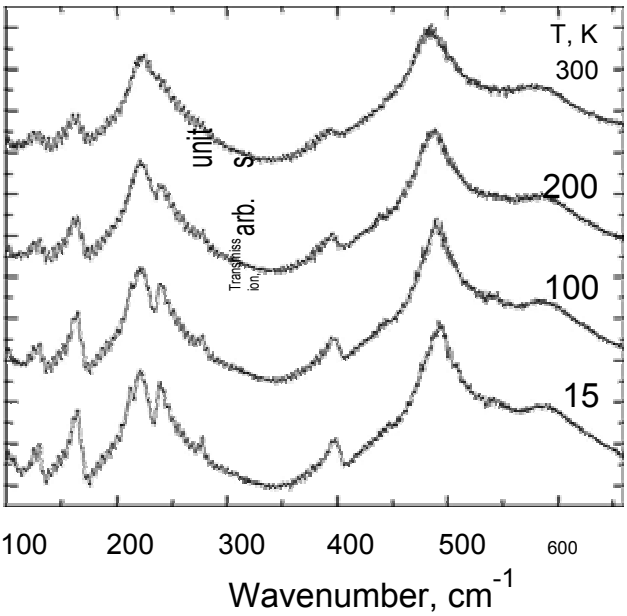

Fig. 10 IR spectra transformation with temperature increasing at Pmmm phase.

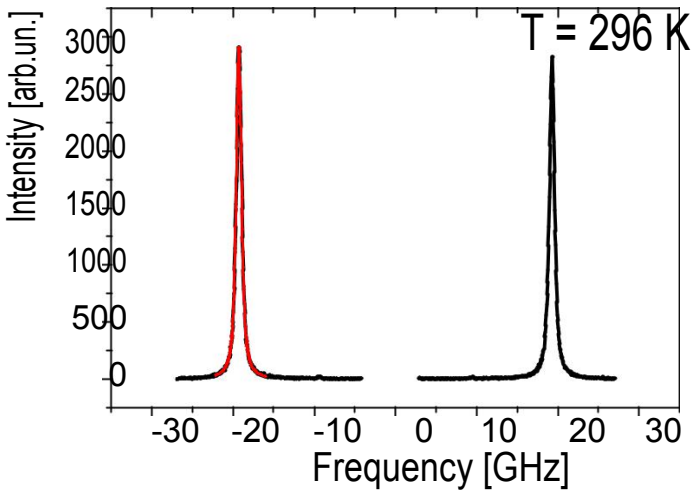

Fig. 11 $CsScF_4$ Brillouin scattering spectrum and fit at 296 K

were changed randomly. The parameters obtained for the Born-Karman model at 543 K are given in Table 7. The structural data of all phases were taken from Tables 4 and 3. Comparison of the simulated and experimental wavenumbers of the Raman lines is presented in Table 8.

4.4 Brillouin light scattering

Fig.11 shows a typical Brillouin scattering spectrum measured in the crystal under study at temperature 296 K. To define positions and linewidths each of the Brillouin components is described by Voigt function with a free Gauss parameter. A fitting example is given in Fig. 11 in red.

Fig. 12 shows the experimentally obtained temperature dependences of the position and width (FWHM) of the Brillouin components. Near 311 K the temperature dependences of both parameters exhibit a distinctive feature indicating a phase transition. Such a behavior is typical for second order structural phase transitions. Another feature is observed as a kink at about 480 K. The magnitude of the effect is relatively small but it allows us to confidently claim the existence of the first order phase transition. The lack of drastic changes in the elastic parameters of the material may be an indication of the lack of changes in the structure of the crystal lattice at this temperature. Such features take place in glasses when additional degrees of freedom of molecules are defrosted during heating of the sample.

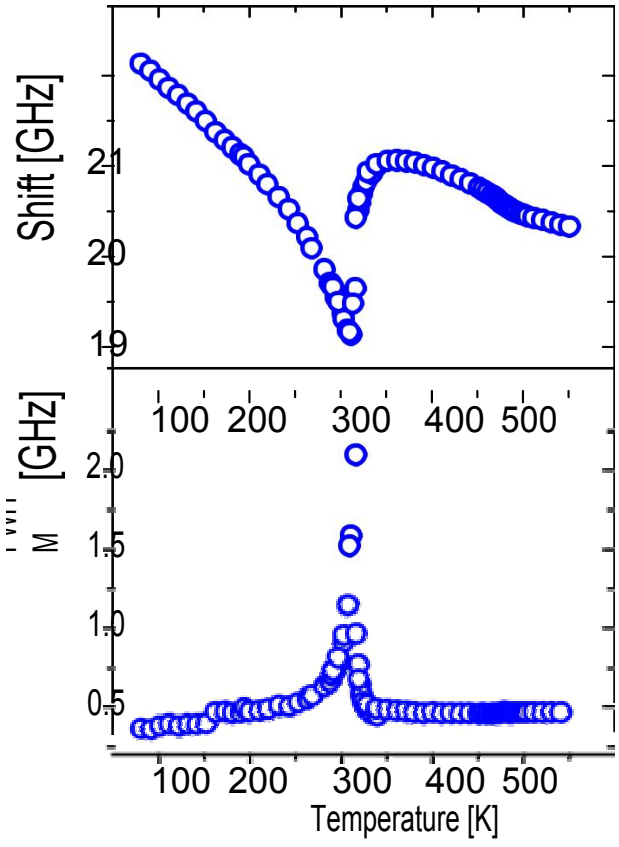

Fig. 12 Temperature dependencies of the position and width (FWHM) of the Brilluoin component

5 NMR

Temperature dependences of ^{19}F NMR spectra were experimentally studied with a single crystal sample in the temperature range 290-585 K. With the external magnetic field oriented along c-axis of the crystal the NMR spectrum of ^{19}F at room temperature con-sists of two lines of equal intensities. When the crystal is rotated around a axis one of these lines splits into two; the splitting is maximal when the magnetic field is normal to c axis. This behav-ior leads to the conclusion that these lines belong to two magneti-cally nonequivalent fluorine atoms in the equatorial plane of ScF_6 octahedron. It is impossible to get parameter values of the chemical shielding tensors from orientation dependences of poorly resolvable NMR spectra of ^{19}F; we can only suppose that they correspond to the polar and equatorial fluorine atoms. Obtained NMR spectra of ^{19}F vary very little in the temperature range from 290 to 510 K, including both phase transitions. Taking into con-sideration the results of X-ray structural studies, such a result is quite expected, because the bond lengths of in the ScF_6 octahe-dron practically do not change in transitions and, accordingly, the parameters of magnetic shielding of fluorine atoms change insignificantly. As for the parameters of dipole-dipole interaction (manifested, first of all, in the width of individual lines) their invariability is indicative of the lack of mobility of fluorine ions in the structure. However, the NMR ^{19}F lines were found to broaden with further heating (above 510 K) and above 530 K all the lines merge into a single line in the centroid of ^{19}F NMR spectrum; its width decreases with increasing temperature (Fig. 13). Such changes in the spectrum are typical of an exchange process, in this case the exchange between polar and equatorial fluorine atoms. The emergence of a single line corresponds to the frequency of exchange approximately equal to the line splitting value in the ^{19}F NMR spectrum.

So, the temperature dependence in Fig. 13 allows the exchange rate n 10^4 Hz to be evaluated at T=530 K. Further narrowing of the lines with increasing temperature is associated with diffusion of fluorine atoms over the crystal lattice sites.

The spin of ^{45}Sc and ^{133}Cs nuclei is I = 7=2 and unlike ^{19}F nuclei, they have electric quadrupole moments. NMR makes it possible to obtain information about the value and symmetry of gradients of crystalline electric fields at the site of the nucleus under study. In the low-temperature phase there is one struc-turally nonequivalent scandium atom (position 4d) in a unit cell. However, in general orientation each of the seven components of the NMR spectrum of ^{45}Sc splits into four lines. Consequently, in a unit cell of $CsScF_4$ there are four magnetically nonequivalent positions of scandium ions. The analysis of orientation depen-dences of the NMR spectrum of ^{45}Sc made it possible to find the three-axial tensor of electric-field gradient (EFG) at the site of scandium ion with the main value V_{ZZ} = 3.41 MHz and asym-metry parameter h 0:1. The principal axis V_{ZZ} of EFG tensor is

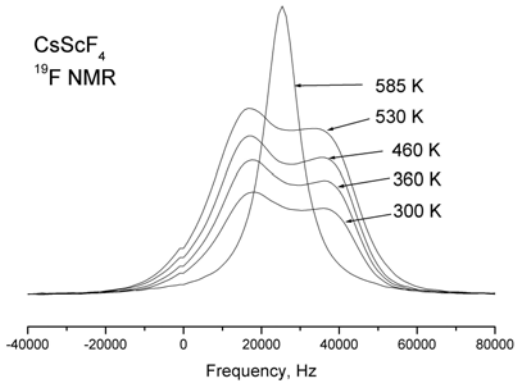

Fig. 13 Temperature evolution of the centroid of ^{19}F spectrum line

tilted from c axis of the crystal by about 10 at room temperature (292 K). Under heating the tilt angle gradually decreases, so does the asymmetry parameter and at phase transition temperature T_2 = 317 K the EFG tensor becomes axially-symmetrical in compliance with the point symmetry of scandium ion position (2b) in the intermediate phase. Fig. 14 shows temperature evolution of ^{45}Sc NMR spectrum lines belonging to transition 3=2 $ 1=2. Over the entire temperature range of existence of the intermediate phase, the principal value of Vzz = 3.41 MHz of the axially symmetrical EFG tensor does not change (Fig. 14). This value does not change in transition to the high-temperature phase (T_1=475 K), either. Even though in this phase transition the point symmetry of scandium position does not change and the distance to the nearest fluorine ions change insignificantly, in the second coordination sphere, according to the X-ray results considerable changes occur which, in principle, should change the V_{ZZ} value. The absence of changes in ^{45}Sc NMR spectra indirectly proves the phase transition model ensuing from the Raman and X-ray data. The changes in the scandium spectrum related to very small structure variation should be very small.

In the low-temperature phase of $CsScF_4$ there are two structurally nonequivalent cesium atoms and, accordingly, two three-axis EFG tensors on Cs nuclei. As a cesium NMR line from each structurally and magnetically nonequivalent position of cesium splits into 7 components, the quadropole splitting is not more than 20 kHz, and tensor parameters are quite close, the resolu-tion in the spectrum is insufficient to accurately define parameters of the said tensors and the tilt angle of their principal axis V_{ZZ} from c axis of the crystal. The phase transition into the intermediate phase (T_2 = 317 K) is clearly recorded by considerable simplification of ^{133}Cs NMR spectra. Analysis of orientation dependences helps to find one axially symmetrical EFG tensor with a

Fig. 14 Temperature evolution of ^{45}Sc NMR spectrum lines

principal value of V_{ZZ} = 20 kHz and direction of the principal axis along c axis. Further increase of temperature up to 510 K does not change the parameters of this tensor. The lack of changes in the cesium spectrum in the first phase transition (475 K) can be explained by the same reasons as in the scandium case, but here the situation is aggravated by much worse resolution associated with small quadropole splittings.

So, the NMR studies on the whole confirm the phase transi-tion model developed on the basis of this Raman scattering and X-ray structural studies. However, it should be noted, that the spectra of none of the nuclei under study exhibit the first phase transition at T=475 K. We assume this to be a consequence of specificity of structural changes taking place at this transition. An additional result is the exchange between equatorial and polar fluorine atoms found in NMR studies of ^{19}F approximately 50 K above the first phase transition. The frequency of this exchange is found to be 20 kHz at 550 K and it grows with temperature.

6 Phase transition thermodynamic model

Critical one-dimensional IR of M2+ induces changes crystal sym-metry at the phase transition of the first order [5,6] another phase transition of the second order is associated with OPs, transformed by two-dimensional IR of X2 . The free energy (FE) correspond-ing to these representations and describing phase transition se-quences can be written as follows:

$$\begin{aligned} F &= F_M + F_X + F_{MX}; \\ F_M &= a_1 h^2 + a_2 h^4 + a_3 h^6; \\ F_M &= a_1 l_1 + a_2 l_1^2 + b_1 l_2 + b_2 l_2^2 + d\, l_1 l_2; \\ F_{MX} &= b h^2 l_1; \\ l_1 &= c_1^2 + c_2^2; \\ l_2 &= (c_1^2 + c_2^2)^2 \end{aligned} \qquad (11)$$

where F_M is the part of potential associated with M2+, F_X is the part of potential associated with X2 , and F_M X, and is the interaction potential, h; c_1; c_2 are the OP components. Below we assume d = 0; it was shown in [48], such an assumption should not significantly affect the results to be produced.

To describe phase transition of the first order F_M – part of FE associated with one-dimensional IRs is written up to the 6-th power of the OP h. This ensues from the necessity of describing phase transition of the first order [46]. For the same reason we as-sume $a_2 < 0$. The other - F_X – part of FE is written up to the 8-th power of the two-component OP (c_1; c_2), as this is the low-est power at which the emergence of all low-symmetry phases occurring in the experiments can be described. [5,6]

Two more restrictions on the TP coefficients are imposed by the condition of existence of global minimum: $a_3 > 0$ and $a_3 > 0$. A similar free energy, but with expansion to the fourth power of h OP was considered in [48]. The given FE was analyzed and phase state diagrams were described in a standard manner similar to the one described in ref. [46] In the case of $CsScF_4$ crystal the transition temperatures are apart from each other by more than 100 degrees, so in (12) we leave the first term of expansion only.

6.1 Possible type of phase diagrams

Fig. 15 and 16 show obtained phase diagrams. First order phase transitions are shown by full lines, and second order phase tran-sitions - by dashed ones; dash-and-dot lines are the boundaries of phase stability for the first order transitions. Thin full lines num-bered 1 and 2 depict a thermodynamic path realized in $CsScF_4$ crystal. Temperatures of observed phase transitions differ consid-erably, so the coefficient b from F_M X should be nonzero and its sign determines the succession of transitions: for positive b the first transition occur into the phase with nonzero h, i.e. phase ((h, 0, 0). Negative b results in the phase (0, c, c). The phase diagrams produced are shifted along a_1 and a_1 against the dia-grams for non-interacting OP h and c by the value proportional to coefficient b. It is possible to transit from the phase (h, 0, 0) into (h, c, c is possible only when $b_1 > 0$. For negative b_1 phase

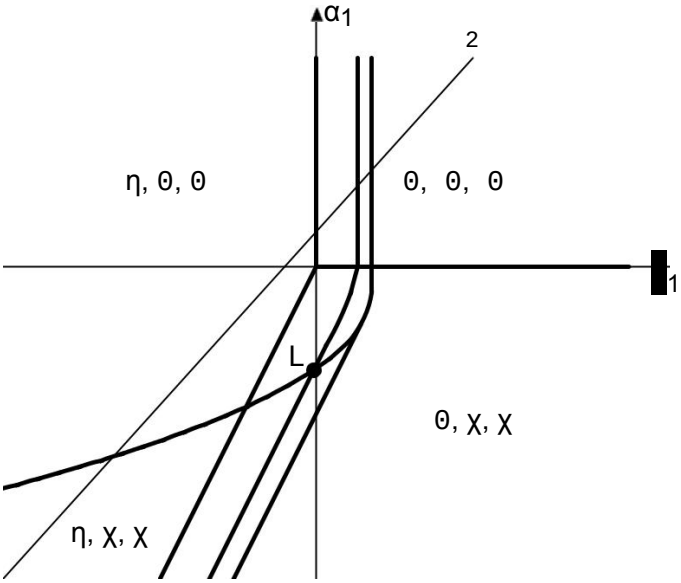

Fig. 15 Diagram of phase state of thermodynamic potential at $a_2 < 0$; $b_2 > 0$; $b > 0$. First order line denoted solid line, second order - dashed, line of bucking phases - dash doted line

(h, 0, 0) transits into phase (h, c, 0). A more detailed examination of the diagram in Fig. 16 shows that the boundary (full line in Fig. 16) of the first order phase transition between phases (h, 0, 0) and (0, c, c) runs along the line

$$a_1 = \frac{3a_3 p_3 r}{2}$$

The stability zone of the phase with OP ((0, c, c) is restricted by the dash-and-dot straight line from the origin of coordinates in Fig. 16. Phases (h, 0, 0) and (h, c, c) are separated by the line of the second order transition $a_1 = a_1(2ba_2\ 3a_1a_3)=b^2$ (dash line). Contrary to [48], the boundary of phase (h, 0, 0) is described by a quadratic equation. $a_1 = \frac{(b^2\ 4a_2a_2)(4a_2a_2+3b^2)}{64a_2^2a_3}$; $a_1 = \frac{b(\ 4a_2a_2+b^2)}{8a_2a_3}$ At the phase diagram there exist a point L with the coordinates: (h, 0, 0), (h, c, c) and (0, c, c) where three phases coexist.

7 Conclusions

We have found relations between the coefficients of thermodynamic potential as a function of order parameters of one-dimensional M2+ and two-dimensional X2 irreducible representations which can occur in layered perovskite $CsScF_4$. Expressions for phase boundaries have been accurately derived from the considered potential. Knowing the pattern of phase states one can conceive how it changes under external influence of differ-ent kind which is necessary for a conscious choice of crystals and understanding possible impacts on them in some applica-tions. The sequence of phase transitions has been reinvestigated:

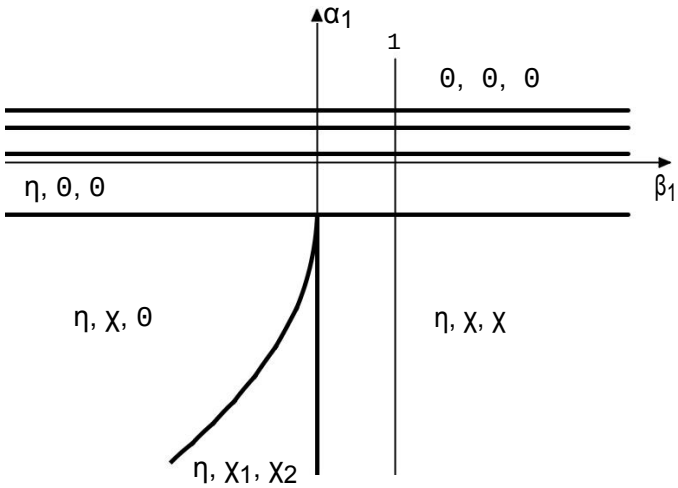

Fig. 16 Diagram of phase state of thermodynamic potential at $a_2 < 0$; $b_2 > 0$; $b_1 > 0$. The full line denotes the first order transition, the dash line denotes the second order, the dash-and-dot line – denotes the bucking phases

M2+(h) M2+(h) X2 (x ;x)
P4=mmm ! P4=mbm , 2! Pmmn

At the first phase transition, ScF_6 octahedrons rotate jumpwise by f h that accounts for the first order transition. There are no other rotations or heavy atom displacements. At the second phase transition, there appear two new rotations are appeared: around

a¯ +b axis on angle y_1 $x_1$and around a¯ b axis on angle y_2 x_2.

Cs1 and Cs2 atoms move along c axis at this second transition. Mechanisms of all phase transitions are of a displacive distortion type. The results of vibrational spectroscopy and NMR studies all in all confirm this phase transition model developed on the basis of the XRD data and thermodynamic model.

8 Acknowledgements

The authors are grateful to Prof. I. N. Flerov for valuable support and useful discussions. This work was partly supported by Russian Foundation for Basic Research, Project 16-02-00102. The research is partially conducted within the framework of the state task of Ministry of Education and Science of the Russian Federa-tion for Siberian Federal University on R&D performance in 2014 (Task 3.2534.2014/K).

References

1 K. S. Aleksandrov, J. Bartolome *Phase Transitions.*, 2001, **74**, 255-336.

2 S. S. P. Parkin , V. Y. Lee, A. I. Nazzal, R. Savoy, R. Beyers, S. J. LaPlaca, *Phys.Rev.Letters.*1988, **61**, 750-753.

3 H. Arend, W. Huber, F. H. Mischgovsky, G. Richter, *J. Crystal Growth.*, 1978, **43**, 213-223.

4 K. S. Aleksandrov, B. V. Beznosikov, *Perovskites: Present and*

Table 1 Principal thermal-physical and crystallographic characteristics of three phases of $CsScF_4$

	G_2	G_1	G_0
PT temperature, K	317.5	475	
Change in the entropy DS/R at PT	0.21	0.16	
Change in the entropy d S/R at PT	0	0.11	
Space group	$D_2^{13}{}_h$ Pmmn	$D_4^5{}_h$ P4=mbm	$D_4^1{}_h$ P4=mmm
Z	4	2	1
T_{exp}, K	200	400	500
Cell parameters			
	$2a_0$	$a_0 + b_0$	a_0
a_i	7.944	5.662	4.025
	$2b_0$	$a_0 + b_0$	b_0
b_i	7.956	5.662	4.025
	c_0	c_0	c_0
c_i	6.763	6.814	6.822

Future. Variety of Parent Phases, Phase Transitions, Possibilities of Synthesis of New Compounds., SB RAS, Novosibirsk, 2004.

5 K. S. Aleksandrov, B. V. Beznosikov, S. V. Misyul, *Ferroelectrics*., 1987, **73**, 201-211.

6 I. N. Flerov, K. S. Aleksandrov, S. V. Melnikova, A. I. Kruglik, S. V. Misjul, B. V. Beznosikov *Ferroelectrics*., 1989, **96**, 175-179.

7 A. Bulou, M. Debiéche, J. Nouet, F. Ganot, C. Dugautier, and P. Moch, *Phase Transitions*, 1991, **33**, 99

8 F. Ganot, M. Papin, A. Bulou, and P. Moch, *Ferroelectrics*, 1991, **124**, 321.

9 M. Papin, A. Bulou, and J. Nouet, *Journal of Physics: Condensed Matter*, 1993, **5**, 3177.

10 M. Couzi, P. L. Loyzance, R. Mokhlisse, A. Bulou, J. L. Four-quet, *Berichte Der Bunsengesellschaft Für Physikalische Chemie*, 1983, **87**, 232.

11 Q. Wang, G. Ripault, A. Bulou, *Phase Transitions*, 1995, **53**, 1.

12 Q. Wang, A. Bulou, A. Desert, *Journal of Physics: Condensed Matter*, 1995, **7**, 825.

13 A. Bulou, J. Nouet, *Journal of Physics C: Solid State Physics*, 1987, **20**, 2885.

14 A. Bulou, M. Rousseau, B. Hennion, *J. Phys.: Condens. Matter*, 1989, **1**, 4553.

15 E. Palacios-Lidón, E. Palacios, R. Burriel, A. Bulou, *Ferroelectrics*, 2002, **270**, 387.

16 B. K. Greve, K. L. Martin, P. L. Lee, P. J. Chupas, K. W. Chapman, A. P. Wilkinson, *J. Am. Chem. Soc.*, 2010, **132**, 15496.

17 C. W. Li, X. Tang, J. A. Munoz, J. B. Keith, S. J. Tracy, D. L. Abernathy, B. Fultz, *Phys Rev Lett*, 2011, **107**, 195504.

18 L. Hu, J. Chen, L. Fan, J. Deng, R. Yu, and X. Xing, *J. Am. Ceramic Society*, 2014, **97**, 1009.

19 O. V. Kovalev, *Irreducible Representations of the Space Groups*, Routledge, 1965

20 S. C. Miller, W. F. Love, *Tables of Irreducible Representations of The Space Groups and Co-Representations of Magnetic Space Groups*, Colorado: Pruett Press Boulder, 1967.

21 V. P. Sakhnenko, V. M. Talanov, G. M. Chechin, *Fiz. Met. Met-alloved*., 1986, **62**, 847-856.

22 A. N. Vtyurin, A. S. Krylov, I. V. Shmygol, A. P. Shebanin, *Phys.Solid State*, 19887, **39**, 632-633.

23 I. C. Madsen, R. J. Hill, *Adv. X-ray Anal.*, 1992, **35**, 39-47.

24 I. C. Madsen, R. J. Hill, *J. Appl. Cryst.*, 1994, **27**, 385-392.

25 W. I. F. David. Abstract P2.6, *NIST Special Publication*, 1992, **846**, 210.

26 Diffrac-Plus Basic XRD Wizard. 2002-2007 Bruker AXS GmbH, Karlsruhe, Germany.

27 A. S. Krylov, E. M. Merkushova, A. N. Vtyurin, L. I. Isaenko, *Phys. Solid State*, 2012, **54** 1275 .

28 A. S Krylov, E. M. Kolesnikova, L. I. Isaenko, S. N. Krylova, A. N. Vtyurin, *Crystal Growth & Design*, 2014, **14**, 923.

29 S. M. Lindsay, M. W. Anderson and J. R. Sandercock, *Rev. Sci. Instrum.*, 1981, **52**, 1478.

30 H. T. Stokes, D. M. Hatch, B. J. Campbell. ISOTROPY (2007) stokes.byu.edu/isotropy.html.

31 B. J. Campbell, H. T. Stokes, D. E. Tanner, D. M. Hatch, *J. Appl. Crystal.*, 2006, **39**, 607.

32 A. N. Vtyurin, A. Bulou, A. S. Krylov, I. V. Shmygol, K. S. Alek-sandrov. *J. Raman Spectros.*, 2000, **31**, 151-155.

33 A. S. Krylov, I. V. Shmygol, A. P. Shebanin, A. N. Vtyurin, A. G. Ageev *Ferroelectrics*, 1999, **233**, 103.

34 I. N. Flerov, M. V. Gorev, J. Grannec, A. Tressaud *J. Fluorine Chemistry.*, 2002, **116**, 9-14.

35 L. H. Hoang, N. T. M. Hien, W. S. Choi, Y. S. Lee, K. Taniguchi, T. Arima, S. Yoon, X. B. Chen, I.-S. Yang, *J. Raman Spectrosc.*, 2010, **41**, 1005.

36 V. K. Malinovsky, A. M. Pugachev, N. V. Surovtsev, *Phys. Solid State*, 2008, **50**, 1137.

Table 2 Main bond lengths of $CsScF_4$

Bond length,	Å
T=133 K, Pmmn	
Sc-F3	1.934(5)
Sc-F1	2.018(4)
Sc-F2	2.049(5)
Cs1-F3	3.07(1)
Cs1-F2	3.27(2)
Cs1-F3	3.30(1)
Cs2-F3	3.07(1)
Cs2-F3	3.29(1)
T=193 K, Pmmn	
Sc-F3	1.935(4)
Sc-F 1	2.026(4)
Sc-F2	2.034(4)
Cs1-F3	3.08(1)
Cs1-F2	3.29(1)
Cs1-F3	3.36(2)
Cs2-F3	3.06(1)
Cs2-F3	3.30(1)
T=253 K, Pmmn	
Sc-F3	1.934(5)
Sc-F1	2.024(5)
Sc-F2	2.033(5)
Cs1-F3	3.10(2)
Cs1-F2	3.28(2)
Cs1-F3	3.41(3)
Cs2-F3	3.07(2)
Cs2-F3	3.30(2)
T=303 K, Pmmn	
Sc-F3	1.926(4)
Sc-F1	2.017(4)
Sc-F2	2.022(5)
Cs1-F3	3.16(2)
Cs1-F2	3.22(2)
Cs1-F3	3.57(3)
Cs2-F3	3.15(2)
Cs2-F3	3.23(2)
T=353 K, P4=mbm	
Sc-F2	1.914(4)
Sc-F1	2.023(6)
Cs-F2	3.196(2)
T=393 K, P4=mbm	
Sc-F2	1.911(5)
Sc-F1	2.020(6)
Cs-F2	3.201(2)
T=433 K, P4=mbm	
Sc-F2	1.902(2)
Sc-F1	2.020(6)
Cs-F2	3.209(2)
T=503 K, P4=mmm	
Sc-F2	1.923(5)
Sc-F1	2.009(1)
Cs-F2	3.207(3)
T=543 K, P4=mmm	
Sc-F2	1.913(5)
Sc-F1	2.013(1)
Cs-F2	3.217(2)
T=583 K, P4=mmm	
Sc-F2	1.913(5)
Sc-F1	2.016(1)
Cs-F2	3.222(2)

37 M. B. Smirnov, V. Yu. Kazimirov, LADY: software for lattice dy-namics simulations. (JINR communications), E 14-2001-159, 2001.

38 M. B. Smirnov, A. P. Mirgorodsky, P. E. Quintard, *J. Mol. Sruct.*, 1995, **348**, 159.

39 A. A. Savina, V. V. Atuchin, S. F. Solodovnikov, Z. A. Solodovnikova, A. S. Krylov, E. A. Maximovskiy, M.S. Molokeev, A. S. Oreshonkov, A. M. Pugachev, E. G. Khaikina, *J. Solid State Chem.*, 2015, **225**, 53-58.

40 A. N. Vtyurin, A. S. Krylov, S. N. Krylova, S. V. Goryainov, V. N. Voronov, A. S. Oreshonkov, *Ferroelectrics*, 2012, **440**, 100-104.

41 A. N. Vtyurin, A. S. Krylov, S. V. Goryainov, S. N. Krylova, A. S. Oreshonkov, V. N. Voronov, *Phys. Solid State*, 2012, **54** 934–936.

42 A. S. Krylov, A. N. Vtyurin, A. S. Oreshonkov, V. N. Voronov, S. N. Krylova, *J. Raman Spectr.* 2013, **44** 763-769.

43 Yu. V. Gerasimova, A. S. Oreshonkov, A. N. Vtyurin, A. A. Iva-nenko, L. I. Isaenko, A. A. Ershov, E. I. Pogoreltsev, *Phys. Solid State*, 2013, **55** 2331–2334.

44 Zhiguo Xia, M.S. Molokeev, A.S. Oreshonkov, V.V. Atuchin, Ru-Shi Liu, Cheng Dong, *Phys. Chem. Chem. Phys.*, 2014, **16** 5952–5957.

45 V. V. Atuchin, A. S. Aleksandrovsky, O. D. Chimitova, T. A. Gavrilova , A. S. Krylov, M. S. Molokeev, A. S. Oreshonkov, B.G. Bazarov, J.G. Bazarova, *J. Phys. Chem. C.* 2014,**118**, 15404-15411.

46 Yu. A. Izyumov, V. N. Syromyatnikov, Phase Transitions and Crystal Symmetry (1990) Springer Netherlands p. 444.

47 I. N. Flerov, K. S. Aleksandrov, S. V. Melnikova, A. I. Kruglik, S. V. Misyul, B. V. Beznosikov, *Ferroelectrics*, 1989, **96**, 175.

48 M. P. Ivliev, V. P. Sakhnenko, *Ferroelectrics*, 1996, **175**, 65-71.

Table 3 Main refinement parameters

T, K	Sp.Gr.	a_i, Å	b_i, Å	c_i, Å	V, Å^3	Z	R_{wp}, %	R_B, %
133	Pmmn	7.9561(5)	7.9545(5)	6.7557(3)	427.55(5)	4	6.26	1.89
193	Pmmn	7.9663(5)	7.9630(4)	6.7668(3)	429.25(4)	4	5.35	1.50
253	Pmmn	7.9783(5)	7.9748(5)	6.7814(3)	431.46(4)	4	5.84	1.52
303	Pmmn	7.9878(5)	7.9832(4)	6.7936(2)	433.21(4)	4	4.43	1.41
353	P4/mbm	5.6538(2)		6.8076(3)	217.60(1)	2	5.97	1.55
393	P4/mbm	5.6601(2)		6.8135(3)	218.28(2)	2	5.50	1.37
433	P4/mbm	5.6667(2)		6.8180(3)	218.94(2)	2	6.21	1.62
503	P4/mmm	4.0175(1)		6.8226(3)	110.117(9)	1	5.91	1.82
543	P4/mmm	4.0260(1)		6.8233(3)	110.599(9)	1	4.94	1.91
583	P4/mmm	4.0317(2)		6.8282(4)	110.99(1)	1	5.15	2.03

Table 4 Fractional atomic coordinates and isotropic (* - equivalent) displacement parameters ($Å^2$) of $CsScF_4$

	x	y	z	Biso, $Å^2$
T=133 K, Pmmn				
Cs1	1/4	1/4	-0.0285(5)	2.5 (1)* U_{11} = 0:054(4);U_{22} = 0:020(4);U_{33} = 0:020(3)
Cs2	1/4	3/4	-0.001(2)	2.6 (1)* U_{11} = 0:023(4);U_{22} = 0:020(4);U_{33} = 0:055(4)
Sc	0	0	1/2	1.4 (1)
F1	1/4	0.540(3)	0.515(3)	1.9 (2)
F2	0.044(3)	1/4	0.552(3)	1.9(2)
F3	0.491(2)	0.469(2)	0.2164(6)	1.9(2)
T=193K,Pmmn				
Cs1	1/4	1/4	-0.0259(5)	3.0(1)* U_{11} = 0:069(3);U22 = 0:020(4);U_{33} = 0:025(3)
Cs2	1/4	3/4	-0.004(2)	3.0 (1)* U11=0.027(3), U22=0.020(4), U33=0.067(3)
Sc	0	0	1/2	1.7 (1)
F1	1/4	0.546(3)	0.515(3)	2.4 (2)
F2	0.032(3)	1/4	0.549(3)	2.4(2)
F3	0.493(2)	0.471(2)	0.2162 (6)	2.4(2)
T=253K,Pmmn				
Cs1	1/4		1/4 -0.0224(8)	3.5(2)* U_{11} = 0:074(5);U_{22} = 0:020(5);U_{33} = 0:037(4)
Cs2	1/4	3/4	-0.005(2)	3.6 (1)* U_{11} = 0:049(5);U_{22} = 0:020(5);U_{33} = 0:066(5)
Sc	0	0	1/2	1.7 (2)
F1	1/4	0.542(4)	0.509(4)	2.7 (2)
F2	0.033(4)	1/4	0.544(4)	2.7(2)
F3	0.494(2)	0.474(2)	0.2166 (6)	2.7(2)
T=303 K, Pmmn				
Cs1	1/4	1/4	-0.0191(6)	4.3(2)* U_{11} = 0:094(5);U_{22} = 0:020(4);U_{33} = 0:047(5)
Cs2	1/4	3/4	0.002(2)	3.55 (1)* U_{11} = 0:061(5);U_{22} = 0:020(4);U_{33} = 0:068(5)
Sc	0	0	1/2	3.9 (2)
F1	1/4	0.539(4)	0.508(4)	3.8 (2)
F2	0.031(4)	1/4	0.523(4)	3.8(2)
F3	0.495(2)	0.486(2)	0.2170 (5)	3.8(2)
T=353 K, P4=mbm				
Cs	0	1/2	0	3.97(8)* U_{11} = U_{22} = 0:036(2);U_{33} = 0:078(2);U_{12} = 0:015(2)
Sc	0	0	1/2	1.9 (1)
F1	0.711(1)	0.211(1)	1/2	4.2 (2)
F2	0	0	0.2189(7)	4.2(2)
T=393 K, P4=mbm				
Cs	0	1/2	0	4.2(1)* U_{11} = U_{22} = 0:038(2);U_{33} = 0:084(2);U_{12} = 0:015(2)
Sc	0	0	1/2	1.9 (1)
F1	0.716(1)	0.216(1)	1/2	4.2 (2)
F2	0	0	0.2195(7)	4.2(2)
T=433 K, P4=mbm				
Cs	0	1/2	0	4.7(1)* U_{11} = U_{22} = 0:043(2);U_{33} = 0:091(2);U_{12} = 0:001(3)
Sc	0	0	1/2	2.0 (2)
F1	0.718(1)	0.218(1)	1/2	4.3 (2)

Table 5 Wyckoff positions and irreducible representations, Raman tensors (G-point phonon modes) for $CsScF_4$ (space groups P4=mmm; P4=mbm; Pmmn).

Atom	Wyckoff position	G-point phonon modes
		P4=mmm (123) D_{4h}^{1}
Cs	1a	$A_{2u} + E_u$
Sc	1d	$A_{2u} + 2E_u + B_{1u}$
F1	2e	$A_{1g} + E_g + A_{2u} + E_u$
F2	2h	$A_{1g} + E_g + 4A_{2u} + 5E_u + B_{1u} + 4B_{2u}$
		Modes classifications
		$G_{Raman} = A_{1g} + E_g$ $G_{IR} = 3A_{2u} + 4E_u$ $G_{Acoustic} = A_{2u} + E_u$ $G_{Mech} = A_{1g} + E_g + 4A_{2u} + 5E_u + B_{1u} + 4B_{2u}$
		Raman tensor
		$A_{1g} = \begin{pmatrix} 0 & a & 0 \\ a & 0 & 0 \\ 0 & 0 & b \end{pmatrix}$ $E_g = \begin{pmatrix} 0 & 0 & e \\ 0 & 0 & 0 \\ e & 0 & 0 \end{pmatrix}$ $E_g = \begin{pmatrix} 0 & 0 & 0 \\ 0 & 0 & e \\ 0 & e & 0 \end{pmatrix}$ $B_{1g} = \begin{pmatrix} c & 0 & 0 \\ 0 & -c & 0 \\ 0 & 0 & 0 \end{pmatrix}$ $B_{2g} = \begin{pmatrix} 0 & d & 0 \\ d & 0 & 0 \\ 0 & 0 & 0 \end{pmatrix}$
		P4=mbm (127) D_{4h}^{5}
Cs	2d	$A_{2u} + 2E_u + A_{1u}$
Sc	2b	$A_{1g} + E_g + A_{2u} + 2E_u + A_{1u} + B_{1u} + B_{1g} + B_{2g}$
F1	4h	$A_{1g} + A_{1u} + A_{2g} + 2E_g + A_{2u} + 2E_u$
F2	4e	
		Modes classifications
		$G_{Raman} = 2A_{1g} + B_{1g} + B_{2g} + 3E_g$ $G_{IR} = 3A_{2u} + 7E_u$ $G_{Acoustic} = A_{2u} + E_u$
		$G_{Meh} = 2A_{1g} + 2A_{1u} + 2A_{2g} + 4A_{2u} + B_{1g} + 2B_{1u} + B_{2g} + 8E_u + 3E_g$
		Raman tensor
		$A_{1g} = \begin{pmatrix} 0 & a & 0 \\ a & 0 & 0 \\ 0 & 0 & b \end{pmatrix}$ $E_g = \begin{pmatrix} 0 & 0 & e \\ 0 & 0 & 0 \\ e & 0 & 0 \end{pmatrix}$ $E_g = \begin{pmatrix} 0 & 0 & 0 \\ 0 & 0 & e \\ 0 & e & 0 \end{pmatrix}$ $B_{1g} = \begin{pmatrix} c & 0 & 0 \\ 0 & -c & 0 \\ 0 & 0 & 0 \end{pmatrix}$ $B_{2g} = \begin{pmatrix} 0 & d & 0 \\ d & 0 & 0 \\ 0 & 0 & 0 \end{pmatrix}$
		Pmmn (59) D_{2h}^{13}
Cs1	2a	$A_g + B_{2g} + B_{3g} + B_{1u} + B_{2u} + B_{3u}$
Cs2	2b	$A_g + B_{2g} + B_{3g} + B_{1u} + B_{2u} + B_{3u}$
Sc	4d	$3A_{1u} + 3B_{1u} + 3B_{2u} + 3B_{3u}$
F1	4e	$2A_g + B_{1g} + B_{2g} + 2B_{3g} + 2B_{1u} + 2B_{2u} + B_{3u} + A_u$
F2	4f	$2A_g + B_{1g} + 2B_{2g} + B_{3g} + 2B_{1u} + B_{2u} + 2B_{3u} + A_u$
F3	8g	$3A_g + 3B_{1g} + 3B_{2g} + 3B_{3g} + 3B_{1u} + 3B_{2u} + 3B_{3u} + 3A_u$
		Modes classifications
		$G_{Raman} = 9A_g + 5B_{1g} + 8B_{2g} + 8B_{3g}$ $G_{IR} = 11B_{1u} + 10B_{2u} + 10B_{3u}$ $G_{Acoustic} = B_{1u} + B_{2u} + B_{3u}$
		$G_{Meh} = 9A_g + 8A_u + 5B_{1g} + 12B_{1u} + 8B_{2g} + 11B_{2u} + 8B_{3g} + 11B_{3u}$
		Raman tensor
		$A_{1g} = \begin{pmatrix} 0 & b & 0 \\ a & 0 & 0 \\ 0 & 0 & c \end{pmatrix}$ $B_{3g} = \begin{pmatrix} 0 & 0 & f \\ 0 & 0 & 0 \\ f & 0 & 0 \end{pmatrix}$ $B_{2g} = \begin{pmatrix} 0 & 0 & 0 \\ 0 & 0 & e \\ 0 & e & 0 \end{pmatrix}$ $B_{1g} = \begin{pmatrix} d & 0 & 0 \\ 0 & -d & 0 \\ 0 & 0 & 0 \end{pmatrix}$

Table 6 Calculated and experimental IR Wavenumbers

Symm. type	Cacl. mode, cm^{-1}	IR, (133K) experiment, cm^{-1}
B_{1u}	8.0	
B_{2u}	8.37	
B_{3u}	8.8	
B_{1u}	11.9	
B_{2u}	12.1	
B_{3u}	12.9	
B_{1u}	82.96	
B_{2u}	85.1	110
B_{1u}	140.3	124
B_{2u}	142.7	127
B_{3u}	145.7	
B_{1u}	146.5	
B_{2u}	164.1	
B_{2u}	165.6	
B_{3u}	167.0	
B_{1u}	168.1	
B_{3u}	186.8	
B_{2u}	188.9	
B_{1u}	195.4	
B_{3u}	203.3	
B_{2u}	219.6	
B_{1u}	223.1	223
B_{2g}	270.9	249
B_{2u}	272.9	
B_{3u}	278.0	
B_{1u}	280.0	392
B_{2u}	503.4	436
B_{3u}	524.7	487
B_{3u}	609.1	
B_{2u}	609.4	
B_{2g}	610.1	587

E_g		155	155

Table 8 Symmetry type and vibration modes at 543 K in P4=mmm phase

symmetry type	normal vibration modes	calculation	experimen
A_{1g}	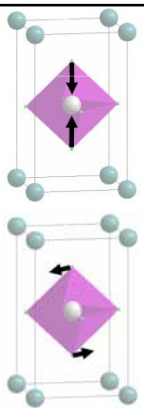	497	492

Table 7 Interatomic interaction potential parameters

Bond	I , [aJ/Å]	r, [Å]
Cs–F	24.45810	0.333473
Sc–F1	199.2600	0.372764
Sc–F2	329.0828	0.384075
F1–F1	308.7130	0.378027
F1–F2	332.7137	0.384993
F2–F2	75.10116	0.349106

Table 9 Symmetry type and vibration modes at 393 K in P4=mbm phase

symmetry type	normal vibration modes	calculation	experimen
E_g	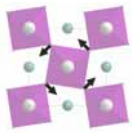	33.6	
A_{1g}		119	
A_{1g}		109.1	
E_g		154.9	
E_g		253.9	
B_{2g}		260.1	
A_{1g}		451.5	
A_{1g}		497.5	

Table 10 Symmetry type and vibration modes at 193 K in Pmmn phase

symmetry type	normal vibration modes	calculation	experiment
A_g	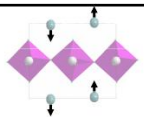	7.7	
A_g		8.2	
B_{3g}		8.4	
B_{3g}		8.6	
B_{2g}	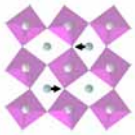	8.9	
B_{2g}	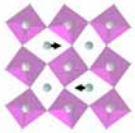	9.1	
A_g		37.2	22.7
B_{3g}		46.0	
A_g		56.6	31.8
B_{2g}		65.2	63
A_g	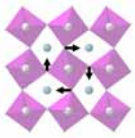	91.5	121
B_{1g}		148.4	
B_{2g}		151.1	154.6
B_{3g}		152.3	157.7
B_{1g}		155.1	
B_{2g}		181.5	182
B_{3g}		183.8	
A_g	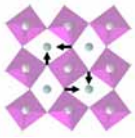	240.9	
B_{3g}		249.3	249.1
A_g		251.5	
B_{2g}		251.5	250.5
A_g		255.7	268.5